

https://dspace.org/

Temperature Dependence of the Hyperfine Magnetic Field at Fe Sites in Ba-Doped BiFeO3 Thin Films Studied by Emission Mössbauer Spectroscopy

Heiniger-Schell, Juliana; Bharuth-Ram, Krish; Naicker, Kimara; Masondo, Vusumuzi; Dang, Thien Thanh ...

2023-04
MDPI
https://hdl.handle.net/10539/49731
Heiniger-Schell, J.; Bharuth-Ram, K.; Naicker, K.; Masondo, V.; Dang, T.T.; Escobar, M.; Díaz-Guerra, C.; Marschick, G.; Masenda, H.; Gunnlaugsson, H.P.; et al. Temperature Dependence of the Hyperfine Magnetic Field at Fe Sites in Ba-Doped BiFeO3 Thin Films Studied by Emission Mössbauer Spectroscopy. Crystals 2023, 13, 724. https://doi.org/10.3390/ cryst13050724

Downloaded from a DSpace repository. https://dspace.org/

crystals

MDPI

Article

Temperature Dependence of the Hyperfine Magnetic Field at Fe Sites in Ba-Doped $BiFeO_3$ Thin Films Studied by Emission Mössbauer Spectroscopy

Juliana Heiniger-Schell [1,2,*], Krish Bharuth-Ram [3,4,*], Kimara Naicker [3], Vusumuzi Masondo [4], Thien Thanh Dang [2], Marianela Escobar [2], Carlos Díaz-Guerra [5], Georg Marschick [6], Hilary Masenda [7], Haraldur P. Gunnlaugsson [8], Bingcui Qi [8], Iraultza Unzueta [9], Sveinn Ólafsson [8], Rajdeep Adhikari [10], Gerrard Peters [7], Deena Naidoo [7], Peter Schaaf [11], Dmitry Zyabkin [11], Karl Johnston [1], Sven Becker [12] and Gerhard Jakob [12]

1 European Organization for Nuclear Research (CERN), CH-1211 Geneva, Switzerland
2 Institute for Materials Science and Center for Nanointegration Duisburg-Essen (CENIDE), University of Duisburg-Essen, 45141 Essen, Germany
3 School of Chemistry and Physics, University of KwaZulu-Natal, Durban 4001, South Africa
4 Physics Department, Durban University of Technology, Durban 4000, South Africa
5 Departmento de Física de Materiales, Facultad de Ciencias Físicas, Universidad Complutense de Madrid, Plaza de Ciencias 1, 28040 Madrid, Spain
6 Institute of Solid State Electronics and Center for Micro- and Nanostructures, Technische Universität Wien, 1040 Vienna, Austria
7 School of Physics, University of the Witwatersrand, Wits 2050, South Africa
8 Science Institute, University of Iceland, Dunhaga 3, IS-107 Reykjavík, Iceland
9 Department of Applied Physics, School of Engineering Gipuzkoa, University of the Basque Country (UPV/EHU), Plaza Europa 1, 20018 San Sebastian, Spain
10 Quantum Materials Group, Institute for Semiconductor and Solid State Physics, Johannes Kepler University, Altenbergerstr. 69, 4040 Linz, Austria
11 Chair Materials for Electrical Engineering and Electronics, Institute of Materials Science and Engineering, Institute of Micro and Nanotechnologies MacroNano®, TU Ilmenau, Gustav-Kirchhoff-Strasse 5, 98693 Ilmenau, Germany
12 Institute of Physics, Johannes Gutenberg University Mainz, Staudinger Weg 7, D-55099 Mainz, Germany
* Correspondence: juliana.schell@cern.ch (J.H.-S.); kbharuthram@gmail.com (K.B.-R.)

Abstract: Emission ^{57}Fe Mössbauer spectroscopy (eMS), following the implantation of radioactive $^{57}Mn^{+}$ ions, has been used to study the temperature dependence of the hyperfine magnetic field at Fe sites in Ba-doped $BiFeO_3$ (BFO) thin films. ^{57}Mn β decays ($t_{1/2}$ = 90 s) to the 14.4 keV Mössbauer state of ^{57}Fe, thus allowing online eMS measurements at a selection of sample temperatures during Mn implantation. The eMS measurements were performed on two thin film BFO samples, 88 nm and 300 nm thick, and doped to 15% with Ba ions. The samples were prepared by pulsed laser deposition on $SrTiO_3$ substrates. X-ray diffraction analyses of the samples showed that the films grew in a tetragonal distorted structure. The Mössbauer spectra of the two films, measured at absorber temperatures in the range 301 K–700 K, comprised a central pair of paramagnetic doublets and a magnetic sextet feature in the wings. The magnetic component was resolved into (i) a component attributed to hyperfine interactions at Fe^{3+} ions located in octahedral sites (B_{hf}); and (ii) to Fe^{3+} ions in implantation induced lattice defects, which were characterized by a distribution of the magnetic field B_{Distr}. The hyperfine magnetic field at the Fe probes in the octahedral site has a room temperature value of B_{hf} = 44.5(9) T. At higher sample temperatures, the B_{hf} becomes much weaker, with the Fe^{3+} hyperfine magnetic contribution disappearing above 700 K. Simultaneous analysis of the Ba–BFO eMS spectra shows that the variation of the hyperfine field with temperature follows the Brillouin curve for $S = 5/2$.

Keywords: Ba-doped bismuth ferrite; emission Mössbauer spectroscopy; hyperfine magnetic field; Néel temperature

check for updates

Citation: Heiniger-Schell, J.; Bharuth-Ram, K.; Naicker, K.; Masondo, V.; Dang, T.T.; Escobar, M.; Díaz-Guerra, C.; Marschick, G.; Masenda, H.; Gunnlaugsson, H.P.; et al. Temperature Dependence of the Hyperfine Magnetic Field at Fe Sites in Ba-Doped $BiFeO_3$ Thin Films Studied by Emission Mössbauer Spectroscopy. *Crystals* **2023**, *13*, 724. https://doi.org/10.3390/cryst13050724

Academic Editors: Anton Meden, Joerg Strempfer, Juliana Schell and Adeleh Mokhles Gerami

Received: 2 March 2023
Revised: 18 April 2023
Accepted: 19 April 2023
Published: 25 April 2023

Copyright: © 2023 by the authors. Licensee MDPI, Basel, Switzerland. This article is an open access article distributed under the terms and conditions of the Creative Commons Attribution (CC BY) license (https://creativecommons.org/licenses/by/4.0/).

1. Introduction

Bismuth ferrite $BiFeO_3$ (BFO) is a well-known multiferroic material with a high antiferromagnetic Néel temperature (T_N = 653 K [1]) and a high ferroelectric Curie temperature (T_C = 1093 K) [2], properties which allow it to be tuned to exhibit the magnetoelectric effect, even at room temperature (RT). Structurally, BFO is a distorted perovskite with the ABO_3 structure. It may appear in three different crystal phases. The α-phase corresponds to a rhombohedral *R3c* structure, with cell parameters a = 5.58 Å and c = 13.90 Å in the hexagonal setting at room temperature [1]. It is a quasi-cubic canted perovskite structure of the $LiNbO_3$ type [1]. This phase exists up to 1093 K, above which a first-order phase transition to the orthorhombic β phase of the *Pbnm* space group sets in [2–4]. Before decomposition, BFO undergoes another phase transition to its γ phase [1].

Although BFO exhibits the magnetoelectric effect at room temperature, as confirmed in measurements with hyperfine interaction techniques [5,6], the magnetoelectric coupling in BFO is too weak for practical applications, due to a modification of the antiferromagnetic G-type spin configuration by a long-range spiral spin superstructure. This spiral spin superstructure cancels the macroscopic magnetization and, thus, prevents a linear magnetoelectric effect. Enhancement of the multiferroic properties of BFO thus requires suppression of the formation of long-range spiral spin cycloids. 'Dopant engineering' is considered an effective way to achieve this goal [7]. Hence, several studies have been conducted to gain a deeper understanding of the origin and nature of magnetism in doped BFO, which may allow one to tailor its magnetoelectrical properties to meet the requirements of specific applications.

The present work aims to contribute to this endeavor by investigating the hyperfine magnetic behavior at ^{57}Fe sites in Ba-doped $BiFeO_3$ (BBFO) through ^{57}Fe emission Mössbauer spectroscopy (eMS). ^{57}FeeMs was selected as a tool due to its extreme sensitivity to both the bonding mechanisms of the Fe probe and the local environment in the vicinity of the probe nuclei, and its distinct signatures for paramagnetic, antiferromagnetic and ferromagnetic interactions. The ^{57}Fe probe nuclei were populated in the β decay of the short-lived radioactive precursor isotope ^{57}Mn ($t_{1/2}$ = 90 s), which was implanted into the samples at the ISOLDE facility [8,9] at CERN. Temperature dependent eMS measurements were conducted online during the Mn implantation, at sample temperatures ranging from room temperature (RT = 301 K) to 700 K.

2. Materials and Methods

2.1. Sample Preparation and Ion Implantation

Two Ba-doped BFO thin film samples, 88 nm and 300 nm thick, and one undoped bulk BFO sample were prepared for the eMS measurements. The undoped, polycrystalline BFO sample was synthesized from a stoichiometric mixture of finely powdered bismuth oxide (Bi_2O_3, 99.9%, Acros Organics) and iron oxide (Fe_2O_3, 99.99%, Alfa Aesar) at the University of Duisburg-Essen [2]. Following calcination of the mixture for 3 h at 1093 K, the resulting powder was pressed into pellets and sintered for 6 h under ambient air at 1093 K. Preparation of the 15% Ba-doped samples was conducted through pulsed laser deposition at the Johannes Gutenberg University Mainz from a sintered target prepared from powders of the respective oxides. The target showed 20% excess Bi (weight %) to compensate for loss during the deposition process. At deposition temperature, the Bi has a high vapor pressure and its sticking coefficient is reduced. The Bi excess was chosen according to energy dispersive composition analysis of deposited films. The thin films were grown on commercial (001) oriented $SrTiO_3$ (STO) single-crystal substrates held at 748 K during deposition. The base pressure in the deposition chamber was 4×10^{-8} mbar, while an oxygen pressure of 0.1 mbar was generated through a 99.95% pure oxygen flow of 10 SCCM, and a partially opened gate valve situated between the deposition chamber and the turbo pump. Focusing the laser onto a 0.1 cm^2 area on the target resulted in an estimated energy density of 640 mJ/cm^2. The laser radiation had a wavelength of 248 nm (Compex Pro205, KrF), the repetition rate was 5 Hz, and the target-to-substrate distance

was 5 cm. The combination of the mentioned parameters resulted in a film growth rate of 1 Å/s. The thin films were grown layer by layer. Atomic force microscopy (AFM) was performed using the Dimension 3100 from Digital Instruments. A surface topography image of a BBFO (300 nm)/STO sample measured by AFM is shown in Figure 1a. The material appears to reproduce the unit cell steps of the STO substrate originating from a miscut. Small islands of BBFO of unit cell height form on the surface, before merging into a continuous layer.

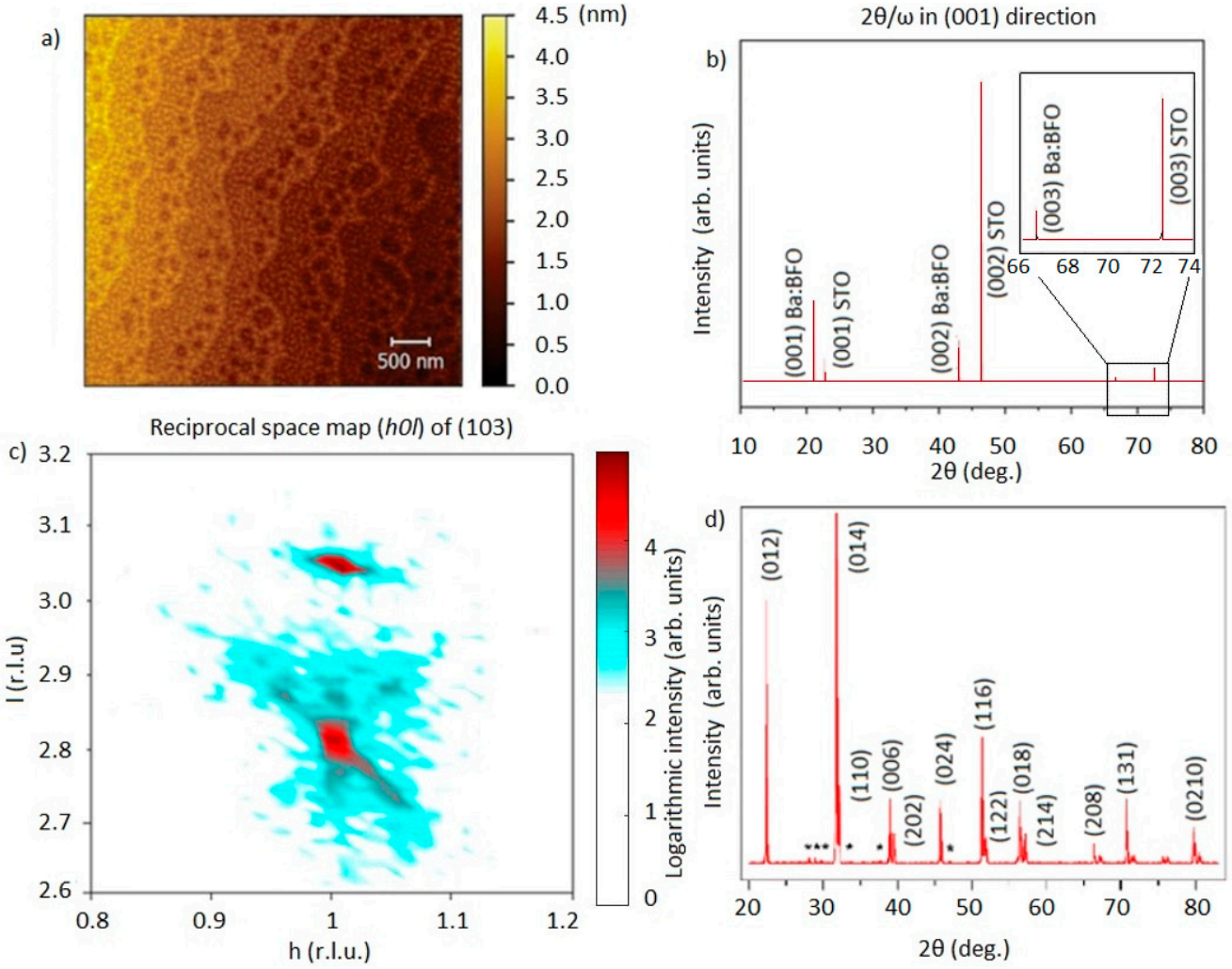


Figure 1. (**a**) AFM image of the surface topography of a BBFO (300 nm)/STO sample; (**b**) its diffractrogram with BBFO peaks labeled in a pseudocubic setting; (**c**) its reciprocal space map in *hl* directions ($k = 0$, fixed) around a (103) diffraction peak (r.l.u. means reciprocal lattice units of the STO substrate); (**d**) diffractogram of the BFO sample, where only the main diffraction maxima of $BiFeO_3$ have been labeled. Minor peaks marked with an asterisk correspond to $Bi_2Fe_4O_9$ secondary phase.

The structural properties of the thin films were characterized by X-ray diffraction (XRD) using a D8 Discover from Bruker. The 2Θ scan in Figure 1b shows that BBFO grows in a single phase with an out-of-plane lattice constant of 4.185 Å. Omega scans of the (001) BBFO reflection reveal a narrow rocking curve of 0.03° FWHM, indicating a well-oriented crystal. The reciprocal space map around the (103) STO substrate peak in Figure 1c shows that BBFO grows fully strained box-on-box on STO in a tetragonal phase with a c/a ratio of 1.07, which coincides with the results reported by Kim and Mix [10,11] for undoped BFO on STO. The structure properties of the BFO undoped ceramic sample were assessed by X-ray diffraction (XRD) on a Philips X'Pert PRO diffractometer using Cu Kα radiation, and by micro-Raman spectroscopy in a Horiba Jovin-Ybon LabRAM HR800 system. The

sample was excited by a 633 nm He-Ne laser on an Olympus BX 41 confocal microscope with a 100× objective. A charge coupled device detector was used to collect the scattered light. The spectral resolution of the system used was ~1 cm^{-1}.

An XRD pattern of the undoped ceramic sample is shown in Figure 1d. The main diffraction maxima match with those of the rhombohedral (R3c) structure of $BiFeO_3$ (PDF file 01-070-5668). Trace amounts of a secondary phase, orthorhombic $Bi_2Fe_4O_9$ (PDF file 01-074-1098), were also detected.

The crystallite sizes of the two thin films were estimated from two 2Θ/ω scans in the (001) direction. As shown in Figure 2a, for the thinner sample, pronounced Laue oscillations are visible between the (001) peak of the thin film and the (001) peak of the substrate. In the *x*-axis, a scaling to the reciprocal lattice of the thin film was chosen so that the position of the (001) substrate peak indicates the $c_{film}/c_{substrate}$ ratio directly. A film thickness of 88.3 nm was calculated from the periodicity of the Laue oscillations.

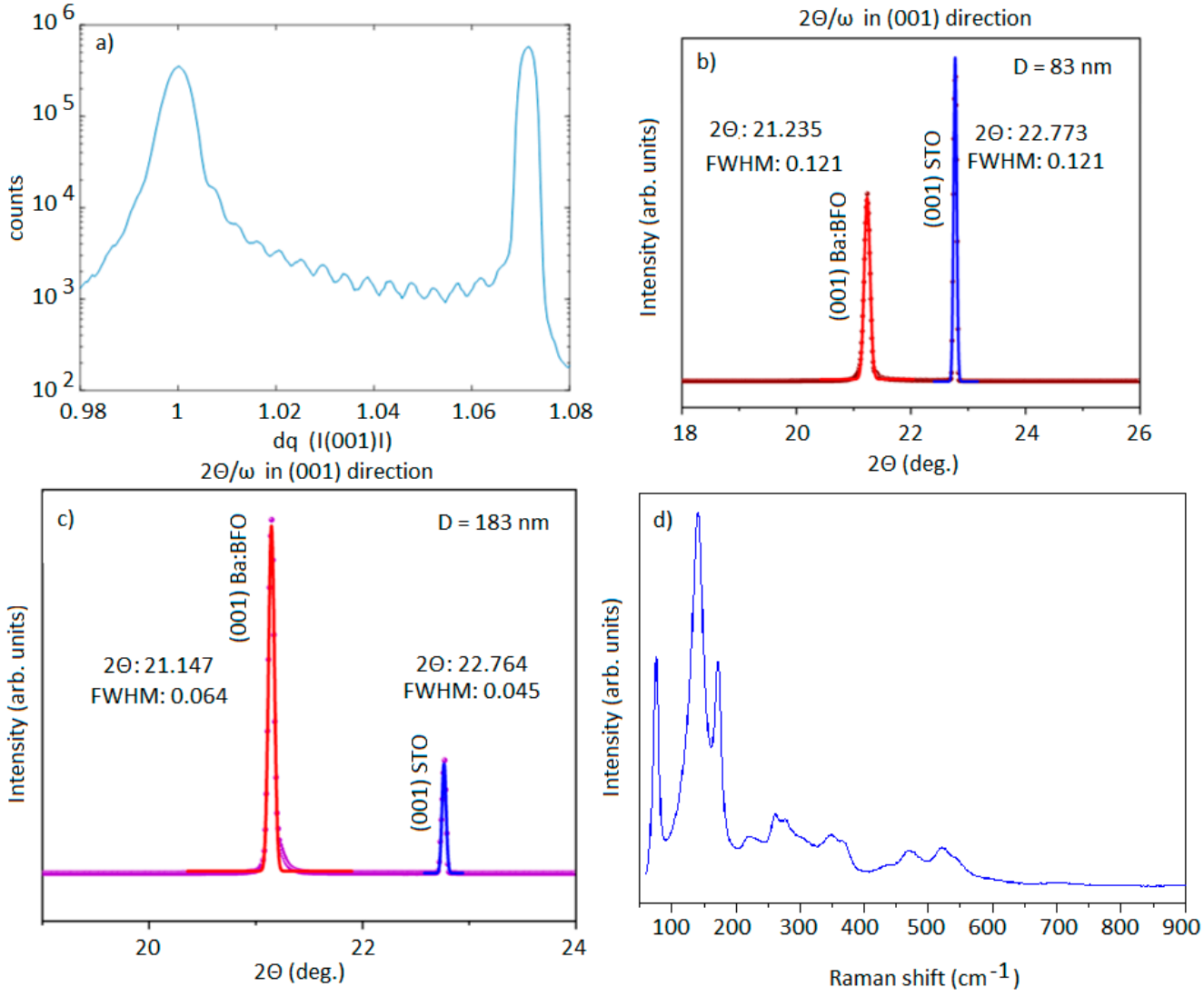


Figure 2. Results of 2Θ/ω scans in the (001) direction for Ba–BFO 88 nm (**a**,**b**) and 300 nm (**c**) films, respectively. In (**a**), the momentum transfer is given in units of the C-axis of the reciprocal space, in order to stress the periodicity of the finite size oscillations, while in (**b**,**c**), conventional angle scaling is used. (**d**) Representative Raman spectrum of the undoped ceramic sample (633 nm excitation).

The Laue oscillations for the thicker film cannot be resolved and, instead, the crystallite size was estimated from the peak width. Figure 2b, for the 300 nm thick Ba–BFO film, shows an FWHM of $\Delta\Theta_{exp} = 0.064°$, and a value of $\Delta\Theta = 0.045°$ for the substrate peak. Taking the

latter value as an estimate of the experimental broadening ($\Delta\Theta_{inst}$), allows an estimate of the size broadening of $\beta = \sqrt{\Theta_{exp}^2 - \Theta_{inst}^2} = 0.046^\circ$, and a corresponding crystallite size of 183 nm, according to the Scherrer equation (Equation (1)) [12]. Similarly, the crystallite size for the thinner film is estimated to be 83 nm. In Equation (1), D is crystallite size; β is the line broadening at half the maximum intensity; λ is the X-ray wavelength; and *K* is a dimensionless shape factor (*K* = 0.94). The deposition rates are only in agreement for the thinner sample crystallite size and film thickness, indicating a fully coherent film growth, while for the 300 nm sample (from the deposition rate), the crystallite size is smaller than film thickness, indicating strain relaxation by defect formation, which is also evident in the slightly different out-of-plane lattice constant.

$$D = \frac{K\lambda}{\beta \cos\theta} \quad (1)$$

Figure 2d shows a representative Raman spectrum of the undoped ceramic sample. Peaks appear centered at 75, 141, 171, 261, 271, 348, 365, 436, 469 and 521 cm^{-1}, and can be attributed to $BiFeO_3$, according to previous reports [13]. A weak peak at about 220 cm^{-1} can be assigned to $Bi_2Fe_4O_9$ [14].

2.2. Emission Mössbauer Spectroscopy (eMS) Measurements

$^{57}Mn^+$ ions were produced at the ISOLDE facility at CERN [8,9], in a fission process induced by 1.4 GeV proton bombardment of a UC_2 liquid-metal target. Following multistage laser ionization and magnetic mass separation, the ^{57}Mn ions were accelerated to 45 keV energy, and implanted into undoped and Ba-doped $BiFeO_3$ (BFO) thin films. ^{57}Mn decays by β^- emission with a half-life of $T_{1/2}$ = 90 s, and feeds the excited 14.4 keV Mössbauer state of ^{57}Fe, thus enabling online ^{57}Fe emission Mössbauer spectroscopy (eMS) measurements [15,16]. The $^{57}Mn \rightarrow {}^{57}Fe$ decay process imparts an average recoil energy of 40 eV to the ^{57}Fe ions, thereby enabling them to substitute Fe ions in the samples under study and become very sensitive probes of the hyperfine fields in their immediate vicinity.

The BFO/Ba–BFO sample was mounted in an implantation chamber at an angle of 30° to the Mn beam direction. The eM spectra were recorded with a parallel plate resonance detector, one electrode of which was made of stainless steel containing enriched ^{57}Fe. The detector was mounted on a drive unit outside the implantation chamber at an angle of 90° to the incident Mn beam, corresponding to a gamma emission angle from the sample of θ_γ = 60° relative to the surface normal [17]. Beam intensities of$\leq 2 \times 10^8$ ions/s were sufficient to give spectra of good statistics, thus ensuring single probe ion implantation and obviating clustering effects. The resonance spectrum at each measurement temperature required 8 min of continuous recording of online data during the ^{57}Mn implantation.

The spectra were analyzed using the analysis code VINDA [18], which allowed simultaneous analysis of the eMS data in each temperature series, with the isomer shift δ of each spectral component constrained to follow a second order Doppler shift with the temperature. The detector velocity scale and the isomer shifts were calibrated with the eM spectrum of an α-Fe foil. The intrinsic spectral line-shape of the resonance detector was a Voigt profile with Lorentzian linewidth $\Gamma_{\mathrm{Det.}}$ = 0.34 mm/s and Gaussian broadening $\sigma_{\mathrm{Det.}}$ = 0.08 mm/s. SRIM estimates [19] of the depth profile of the Mn ions and of the Bi, Fe and O vacancies produced by each implanted ion are shown in Figure 3.

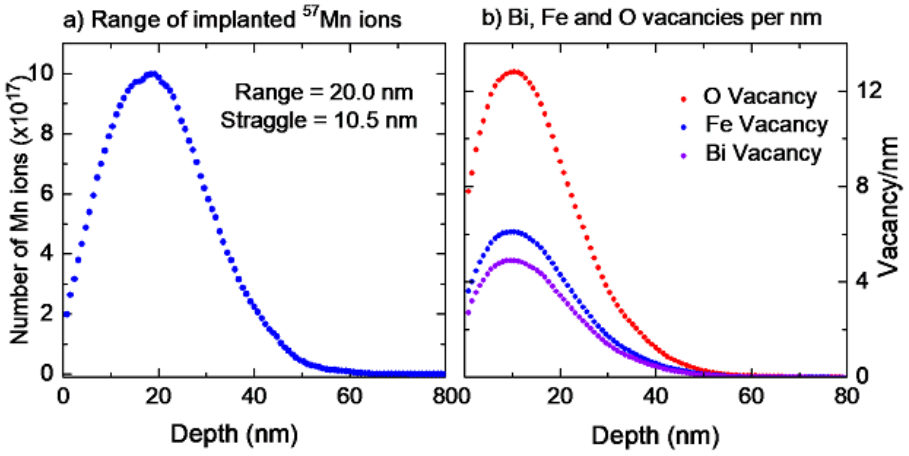


Figure 3. SRIM estimates of (**a**) the implantation profile of the Mn ions and (**b**) the profile of Bi, Fe and O vacancies produced by each implanted Mn ion.

The estimates yield a peak concentration of implanted Mn ions at 20.0 nm from the sample surface, with a straggle of 10.5 nm. Each implanted Mn ion is estimated to produce approximately 500 vacancies, the majority of which, as shown in Figure 3, are oxygen vacancies.

3. Results

The eM spectra collected at room temperature from the undoped pellet, and the two Ba-doped $BiFeO_3$ films are shown in Figure 4. The spectra are plotted against the detector velocity and, hence, have the velocity sign reversed in comparison to conventional transmission MS measurements with a moving source.

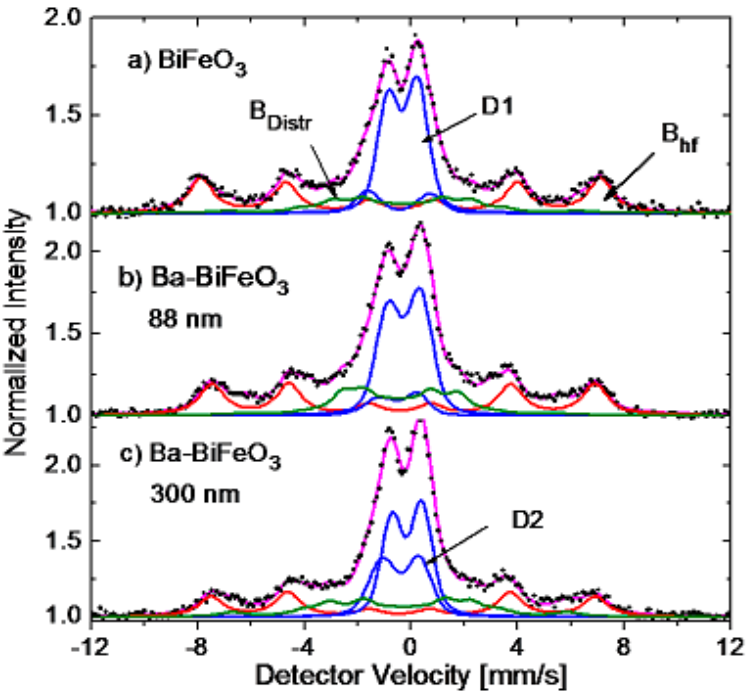


Figure 4. Emission Mössbauer spectra (**a**) of the undoped $BiFeO_3$ pellet, and (**b**,**c**) of the Ba-doped 88 nm and 300 nm thick $BiFeO_3$ films, respectively, collected at room temperature. Colorful solid lines correspond to the different fitting components.

Each spectrum in Figure 4 is characterized by a strong central paramagnetic component and a broad sextet feature. The central component was resolved into two quadrupole split

doublets (D1 and D2), with fit parameters (isomer shift (δ) and quadrupole splitting (ΔE_Q)) listed in Table 1. These values are quite different to those reported by Papaefthymiou et al. for $Bi_2Fe_4O_9$ [20], and rule out such contaminant in our thin film samples. The sextets observed in the present study are broader than those observed in transmission Mössbauer measurements [10,21]. In addition, the intensities between the sextet peaks do not approach the background, attesting to the implantation induced lattice damage in our data, in particular lattice vacancies, as reflected in Figure 3. Kim et al. resolved the magnetic sextets into two primary components, attributed to Fe on octahedral sites and in octahedral sites with neighboring oxygen vacancies. However, in a recent study on Co-doped $BiFeO_3$, Sobolev et al. [21] argue that the lack of direct experimental evidence discounts the formation of two magnetic sites for Fe ions in $BiFeO_3$. Instead, they propose that spatially ordering spin modulations in BFO at temperatures below the Néel temperature need to be taken into account. In their analysis, a bunched spiral model of spin ordering was found to provide very good fits to their experimental Mössbauer spectra. As already alluded to, the present online ion-implantation eMS study is beset with a range of lattice defects produced by the energetic Mn ions. Fe probes located in these lattice defects experience a distribution of magnetic hyperfine fields, and are a significant contributor to the eMS spectra. Accordingly, the sextet components observed in our spectra were analyzed in terms of (i) a symmetric magnetic hyperfine component (B_{hf}), due to Fe in octahedral sites (Site 1); and (ii) a magnetic distribution component, due to Fe probes located in lattice defect sites, B_{Distr} (Site 2). The data in each temperature series was analyzed in a simultaneous fit, with the isomer shifts constrained to follow a second order Doppler shift with increasing temperature. The fit parameters of the spectral components of the eMS spectra of the three samples, at room temperature, are listed in Table 1.

Table 1. Room temperature fit parameters (isomer shift δ, electric quadrupole splitting/shift ($\Delta E_Q/\varepsilon$), hyperfine magnetic field (B_{hf}) or (B_{Distr}) and area fraction (A)) of the spectral components required to fit the eM spectra of the undoped and Ba-doped BFO samples. The isomer shifts are given relative to an α-Fe absorber.

Sample	Spectral Component	δ (mm/s)	$\Delta E_Q/\varepsilon$ (mm/s)	B_{hf} (T)	Area Fraction (%)
$BiFeO_3$	D1	0.31(1)	1.10(1)	-	35(1)
	D2	0.45(1)	2.3(2)	-	7(1)
	B_{hf}	0.37(1)	0.033(3)	46.3(3)	32(1)
	B_{Distr}	0.32(5)	0.015(4)	40-16	26(2)
Ba-$BiFeO_3$ 88 nm	D1	0.45(6)	1.66(2)	-	7(1)
	D2	0.26(1)	1.20(1)	-	35(1)
	B_{hf}	0.35(1)	0.14(2)	44.5(9)	30(1)
	B_{Distr}	0.42(4)	0.04(5)	37-13	29(2)
Ba-$BiFeO_3$300 nm	D1	0.38(3)	1.38(4)	-	19(1)
	D2	0.16(1)	1.12(1)	-	29(1)
	B_{hf}	0.37(2)	0.15(3)	44.6(2)	21(1)
	B_{Distr}	0.35(4)	0.12(5)	39-16	31(2)

The isomer shifts of the magnetic and paramagnetic components at room temperature are all characteristic of the ferric (Fe^{3+}) state [22], thus eliminating any contaminant Fe^{2+} and Fe^{4+} components in our samples. The measured hyperfine field, B_{hf}, for all three samples, are typical of the Fe^{3+} ion in high spin S = 5/2 configuration.

The series of temperature dependent measurements on the 88 nm and 300 nm thick Ba-doped $BiFeO_3$ films, together with their spectral components, are shown in Figure 5a,b. With increasing temperature, the spectra become increasingly dominated by the central doublet feature. As a consequence, the spectra are presented on an expanded vertical scale to facilitate the study of the main magnetic components.

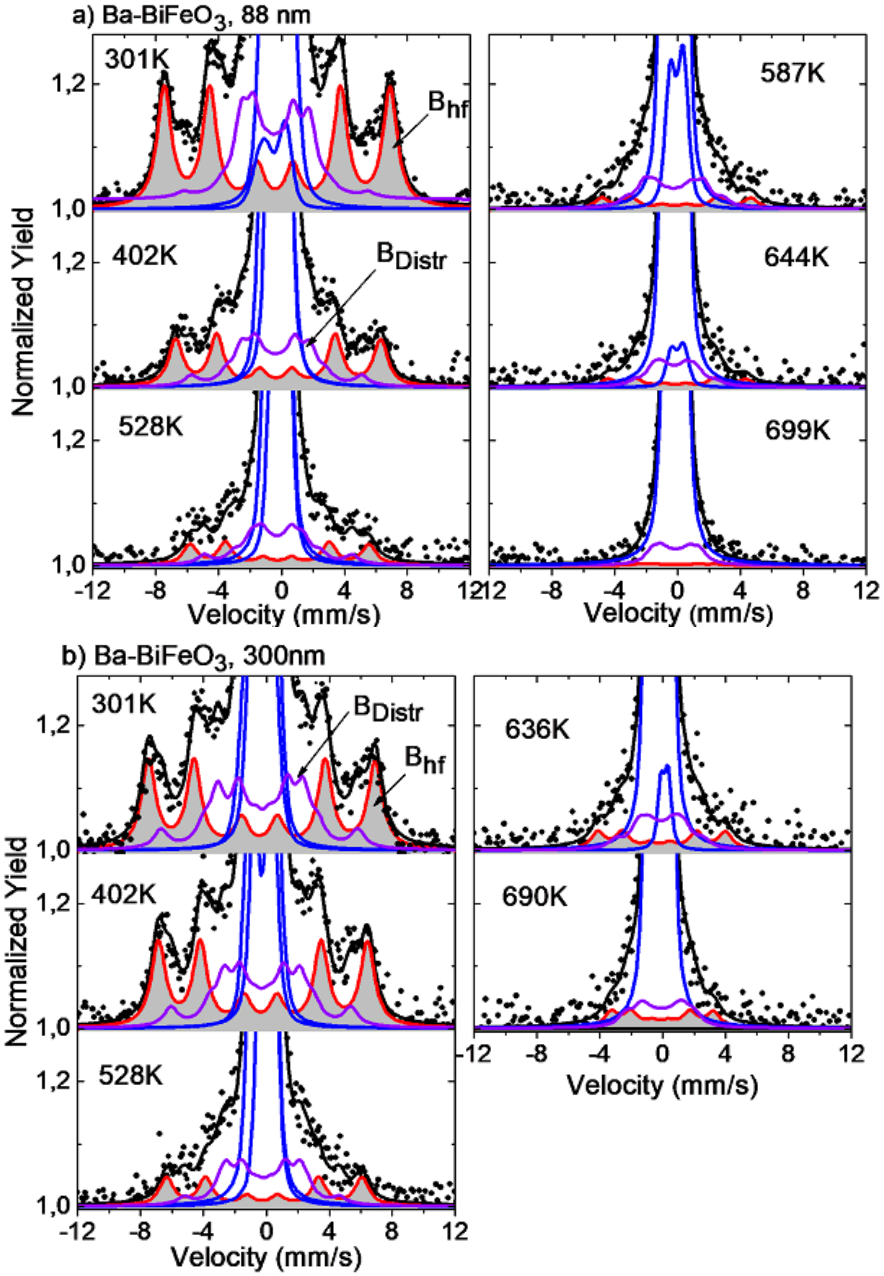


Figure 5. Emission Mössbauer spectra of (**a**) the 88 nm thick and (**b**) the 300 nm thick BBFO films, collected at the indicated temperatures. The spectra are drawn on an expanded vertical scale to better display the magnetic spectral components; the primary B_{hf} sextet is shaded in grey.

The temperature dependence of the areal fractions of the spectral components is presented in Figure 6. The contribution of the primary sextet component (B_{hf}) to the total spectral area decreases from 34% at RT to 4% at 640 K for the 88 nm sample, and from 21% to 6% over the same temperature interval for the 300 nm sample. While accurate analyses of the weaker individual components at the higher temperatures become more difficult, the simultaneous fit to the data in each temperature series using a set of macros described in the analysis code VINDA [18] overcomes these shortcomings.

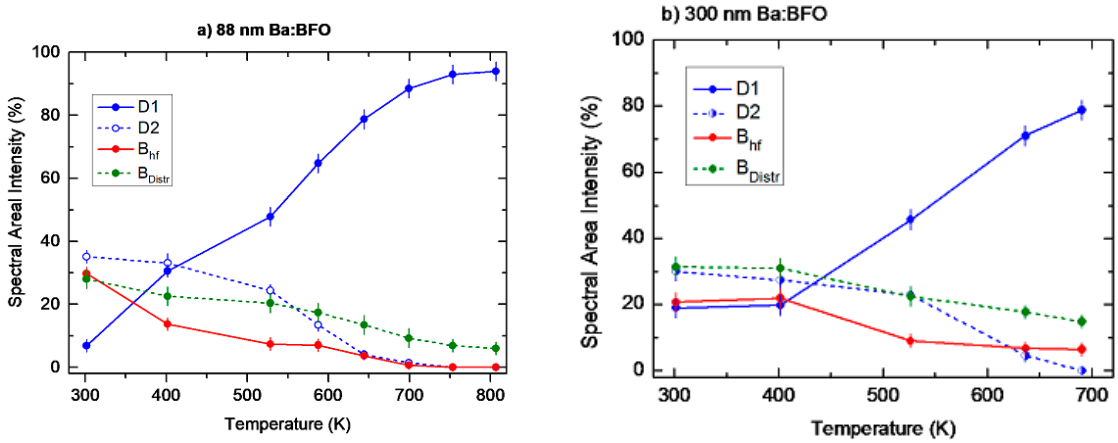


Figure 6. Site population of the spectral components of the (**a**) 88 nm and (**b**) 300 nm Ba-doped BFO films.

The strong difference between the contributions of the paramagnetic doublets (D1, D2) to the eM spectra of the two doped BFO samples is also notable, with D1 contributing a low 7% at 300K to the total spectral area of the 88 nm thick sample, compared to its 19% contribution for the 300 nm sample. The contribution of the B_{hf} component to the spectra also decreases more rapidly with increasing temperature for the 88 nm sample.

At a temperature above 690 K, the magnetic components collapse into a paramagnetic doublet with hyperfine parameters isomer shift (δ) and quadrupole splitting (ΔE_Q) values of 0.17(1) mm/s and 0.90 mm/s, respectively, for the 88 nm film, and corresponding values of 0.13 mm/s and 0.74 mm/s for the 300 nm film. Similar observations have been reported by Kothari et al. (δ = 0.2 mm/s, ΔE_Q = 0.5 mm/s) in Mn-doped BFO [23]

Temperature Dependence of the Hyperfine Magnetic Field B_{hf}

The $^{57}Mn \rightarrow {}^{57}Fe$ β decay imparts to the ^{57}Fe Mössbauer probe nucleus an average recoil energy of approximately 40 eV, which allows the probe nuclei to replace Fe ions in octahedral sites in the lattice, as well as to become trapped in lattice defects, where they experience a distribution of magnetic fields. Fe in the defect sites comprises part of the eM spectra, which are then fit with an additional component, B_{Distr}, comprising a distribution of magnetic fields. Describing the magnetic temperature behavior thus primarily involves the temperature dependence of the hyperfine magnetic component B_{hf}. This is presented in Figure 7 for the BFO/Ba–BFO samples.

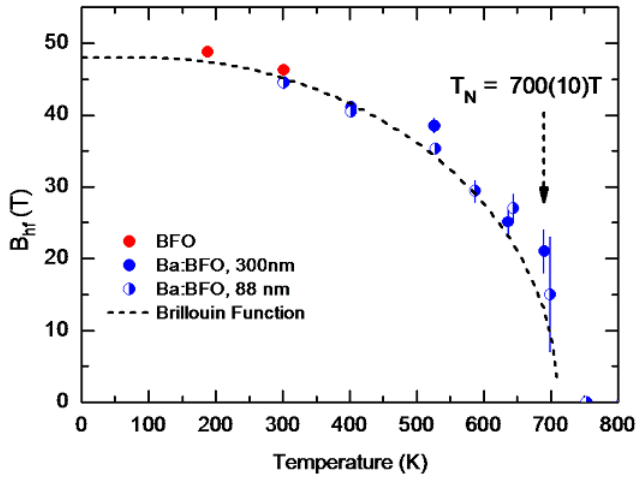


Figure 7. The hyperfine magnetic field strength of spectral component B_{hf} of the doped and undoped BFO samples as a function of temperature. The dashed grey line represents the Brillouin function for high spin S = 5/2.

At higher temperatures, the intensities of the sextet components are considerably reduced, and the B_{hf} values are determined with relatively large errors. Nevertheless, the results of this study are consistent with the Brillouin curve for high spin S = 5/2.

4. Discussion

The magnetic and ferroelectric properties of BFO change significantly upon Ba^{2+} substitution in place of Bi^{3+}. This substitution affects the centrosymmetry of the FeO_6 octahedra. The resulting oxygen vacancies lead to changes of the multiferroic properties of $BiFeO_3$ [24]. Spin canting, coupled with the displacement of oxygen atoms from their original lattice sites, could then be responsible for the observed enhanced magnetic and ferroelectric properties of this material [25]. The two Ba-doped BFO thin films used in our study are fully strained and have a tetragonal structure. By optical second harmonic generation, Kumar et al. reported that there is co-existence of the tetragonal and rhombohedral phases in strained bismuth ferrite films [26]. Our results are consistent with this scenario.

Another explanation for the origin of the hyperfine magnetic field could be that, by doping with Ba^{2+} ions, the structure of the sample may be distorted by the formation of oxygen vacancies. Upon replacing Bi^{3+} ions by Ba^{2+} ions in the lattice site, the system is destabilized due to charge imbalance. In this process, one oxygen vacancy is created to stabilize the system.

Eventually, the replacement of Bi^{3+} by Ba^{2+} is balanced by switching Fe^{2+} to Fe^{3+} [27]:

$$Bi^{3+} + Fe^{2+} \rightarrow Ba^{2+} + Fe^{3+}. \quad (2)$$

The presence of oxygen vacancies and epitaxial strain may change the bond angle and the Fe–O–Fe distance, creating a net magnetization in the sample [28]. Some researchers attribute the onset of ferromagnetism in BBFO nanostructures to the suppression of spiral spin order and structural distortion by Ba doping, which are quantified as changes in the Fe–O–Fe bond angle [29–31]. The change in bond angle modifies the tilting angle of the FeO_6 octahedron, which may suppress the cycloid spin structure and thus produce a net magnetization in the BBFO nanoparticles [27].

The macroscopic magnetization of BFO is eliminated by the incommensurate cycloid spin modulation with a wavelength of 62 nm [32]. Some studies report that the magnetic properties are favored by uncompensated spins if the typical crystallite size is reduced below 62 nm, because the spiral spin structure can be partially destroyed [33,34]. This will result in inferior ferromagnetic behavior, because the long wavelength of BFO thin film is partially destroyed, causing identifiable, incomplete and uncompensated spins [35,36]. As shown in Figure 2, the crystallite sizes of both thin films are larger than 62 nm, so enhanced hyperfine magnetic field of the Ba–BFO samples in this study cannot be ascribed to a reduced crystallite size. In addition, the substrate can influence the cycloid type [37].

In the transmission Mössbauer spectra of BFO samples, the sextets are assumed to come from either iron ions on two different lattice sites [10] or Fe in a site where they experience a bunched spiral ordering of spin [21]. In the present study, B_{hf} and $B_{distribution}$ are attributed to Fe ions at octahedral sites (Site 1) and at defect sites (Site 2) induced by the implantation process. The Mössbauer parameters of the B_{hf} subspectrum for 88 nm thick (300 nm thick) Ba–BFO samples at room temperature are δ = 0.35(1) mm/s δ = 0.37(2) mm/s); quadrupole splittings ΔE_Q = 0.14(2) mm/s (ΔE_Q = 0.15(3) mm/s); and hyperfine magnetic fields B_{hf} = 44.5(9) T (B_{hf} = 44.6(2) T). The measured hyperfine fields are typical for ferric iron (Fe^{3+}) in a high-spin configuration. The isomer shift δ at room temperature is δ = 0.35(1) mm/s relative to α-Fe metal, which is consistent with the ferric state (Fe^{3+}) in oxide materials [38,39]. This isomer shift differs from that of Fe^{4+} (δ = 0.089 mm/s), which suggests that our BBFO compound has no Fe^{4+} ions. Therefore, the substitution of divalent Ba for trivalent Bi in the single-phase Ba–BFO compound may only induce oxygen vacancies in the lattice.

5. Conclusions

The relative contributions of the spectral components required to analyze the eMS data on Ba-doped 88 nm and 300 nm thick BFO layers reflect the effects of the online ion implantation procedure in our measurements on the two samples. However, the hyperfine magnetic field B_{hf} sensed by the ^{57}Fe probe in the samples follows the same temperature dependence, with a pattern similar to that of pure BFO (Néel temperature T_N = 653 K) [1], which is indicative of the magnetic order existing in our Ba-doped BFO samples.

The temperature dependence of the hyperfine field B_hf is consistent with the Brillouin curve for high spin S = 5/2 (Figure 7), with the temperature at which B_{hf} = 0 estimated to be close to 700 K, a value higher than the Néel temperature of BFO. Similar increases in T_N of doped $BiFeO_3$ have been reported by Catalan et al. [40] and Suresh et al. [41]. For Ca doping, Catalan et al. reported an increase of 0.66 K per dopant percentage, while Suresh et al. reported an increase of the T_N in La-doped BFO towards that of $LaFeO_3$ (738 K).

Author Contributions: J.H.-S., K.B.-R., V.M., K.N., T.T.D. and G.M. wrote the manuscript and are responsible for data analysis, J.H.-S., K.B.-R., K.N., H.M., H.P.G., I.U., S.Ó., R.A., G.P., D.N., P.S., D.Z., K.J., S.B., C.D.-G., G.J., B.Q. and M.E. are responsible for the measurements. All authors have read and agreed to the published version of the manuscript.

Funding: This work has received the financial support from the Federal Ministry of Education and Research (BMBF) through grants 05K16PGA, 05K22PGA, 05K16SI1, 05K19SI1 "eMIL" and "eMMA"; from the European Union's Horizon 2020 Framework research and innovation program under grant agreement no. 654002 (ENSAR2) and 101057511 (EURO-LABS); from the Ministry of Economy and Competitiveness Consolider—Ingenio Project CSD2009 0013 "IMAGINE" Spain, and Banco Santander-UCM, project PR87/19-22613; from the Austrian Science Fund (FWF) through projects P26830 and P31423, from the Icelandic University Research Fund; from the National Research Foundation (South Africa); and from the Ministry of Economy and Competitiveness (MINECO/FEDER) for the Grant No. RTI2018-094683-B-C55 C55 and Basque Government Grant No. IT-1500-22.

Institutional Review Board Statement: Not applicable.

Informed Consent Statement: Not applicable.

Data Availability Statement: The data are available from the authors upon reasonable request.

Acknowledgments: We acknowledge the financial support received from the Federal Ministry of Education and Research (BMBF) through grants 05K16PGA, 05K22PGA, 05K16SI1, 05K19SI1 "eMIL" and "eMMA". We also acknowledge the support of all the technical teams at ISOLDE for their excellent work in delivering high-quality beams for emission Mössbauer measurements. We acknowledge the support of the European Union's Horizon 2020 Framework research and innovation program under grant agreement no. 654002 (ENSAR2) and 101057511 (EURO-LABS). We thank the Ministry of Economy and Competitiveness Consolider—Ingenio Project CSD2009 0013 "IMAGINE" Spain, and Banco Santander-UCM, project PR87/19-22613. We also acknowledge the Austrian Science Fund (FWF) through projects P26830 and P31423. We are grateful for the support from the Icelandic University Research Fund. K. Bharuth-Ram, H. Masenda, D. Naidoo and K Naicker acknowledge support from the National Research Foundation (South Africa), I. Unzueta would like to acknowledge the support of the Ministry of Economy and Competitiveness (MINECO/FEDER) for the Grant No. RTI2018-094683-B-C55 and C55 and Basque Government Grant No. IT-1500-22.

Conflicts of Interest: The authors declare no conflict of interest.

References

1. Catalan, G.; Scott, J.F. Physics and Applications of Bismuth Ferrite. *Adv. Mater.* **2009**, *21*, 2463–2485. [CrossRef]
2. Marschick, G.; Schell, J.; Stöger, B.; Gonçalves, J.N.; Karabasov, M.O.; Zyabkin, D.; Welker, A.; Escobar, C.M.; Gärtner, D.; Efe, I.; et al. Multiferroic bismuth ferrite: Perturbed angular correlation studies on its ferroic $\alpha-\beta$ phase transition. *Phys. Rev. B* **2020**, *102*, 224110. [CrossRef]
3. Arnold, D.C.; Knight, K.S.; Morrison, F.D.; Lightfoot, P. Ferroelectric-Paraelectric Transition in $BiFeO_3$: Crystal Structure of the Orthorhombic β Phase. *Phys. Rev. Lett.* **2009**, *102*, 027602. [CrossRef]
4. Wei, J.; Wu, C.; Yang, T.; Lv, Z.; Xu, Z.; Wang, D.; Haumont, R.; Cheng, Z. Temperature-Driven Multiferroic Phase Transitions and Structural Instability Evolution in Lanthanum-Substituted Bismuth Ferrite. *J. Phys. Chem.* **2019**, *123*, 4457–4468. [CrossRef]

5. Schell, J.; Schmuck, M.; Efe, I.; Dang, T.T.; Gonçalves, J.N.; Lewin, D.; Castillo, M.E.; Shvartsman, V.V.; Costa, Â.R.G.; Köster, U.; et al. Strong magnetoelectric coupling at an atomic nonmagnetic electromagnetic probe in bismuth ferrite. *Phys. Rev. B* **2022**, *105*, 094102. [CrossRef]
6. Dang, T.T.; Schell, J.; Boa, A.G.; Lewin, D.; Marschick, G.; Dubey, A.; Escobar-Castillo, M.; Noll, C.; Beck, R.; Zyabkin, D.V.; et al. Temperature dependence of the local electromagnetic field at the Fe site in multiferroic bismuth ferrite. *Phys. Rev. B* **2022**, *106*, 054416. [CrossRef]
7. Yang, C.-H.; Kan, D.; Takeuchi, I.; Nagarajan, V.; Seidel, J. Doping $BiFeO_3$: Approaches and enhanced functionality. *Phys. Chem. Chem. Phys.* **2012**, *14*, 15953–15962. [CrossRef] [PubMed]
8. Catherall, R.; Andreazza, W.; Breitenfeldt, M.; Dorsival, A.; Focker, G.; Gharsa, T.; Giles, T.; Grenard, J.; Locci, F.; Martins, P.; et al. The ISOLDE facility. *J. Phys. G* **2017**, *44*, 094002. [CrossRef]
9. Johnston, K.; Schell, J.; Correia, J.; Deicher, M.; Gunnlaugsson, H.; Fenta, A.; David-Bosne, E.; Costa, A.; Lupascu, D.C. The solid state physics programme at ISOLDE. *J. Phys. G* **2017**, *44*, 104001. [CrossRef]
10. Kim, W.; Kim, C.S. Mössbauer study of polycrystalline multiferroic Ba-doped $BiFeO_3$ compound. *J. Kor. Phys. Soc.* **2010**, *56*, 607–610. [CrossRef]
11. Mix, C.; Jakob, G. Multiferroic and structural properties of $BiFeO_3$ close to the strain induced phase transition on different substrates. *J. Appl. Phys.* **2013**, *113*, 17D907. [CrossRef]
12. Patterson, A.L. The Scherrer Formula for X-ray Particle Size Determination. *Phys. Rev.* **1939**, *56*, 978–982. [CrossRef]
13. Porporati, A.A.; Tsuji, K.; Valant, M.; Axelsson, A.-K.; Pezzottia, G. Raman tensor elements for multiferroic $BiFeO_3$ with rhombohedral *R3c* symmetry. *J. Raman Spectrosc.* **2010**, *41*, 84–87. [CrossRef]
14. Iliev, M.; Litvinchuk, A.; Hadjiev, V.G.; Gospodinov, M.M.; Skumryev, V.; Ressouche, E. Phonon and magnon scattering of antiferromagnetic $Bi_2Fe_4O_9$. *Phys. Rev. B* **2010**, *81*, 024302. [CrossRef]
15. Weyer, G.; ISOLDE Collaboration. Mössbauer spectroscopy at ISOLDE. *Hyperfine Interact.* **2000**, *129*, 371–390. [CrossRef]
16. Weyer, G. Defects in semiconductors—Results from Mössbauer spectroscopy. *Hyperfine Interact.* **2007**, *177*, 1–13. [CrossRef]
17. Schell, J.; Zyabkin, D.; Bharuth-Ram, K.; Gonçalves, J.N.; Díaz-Guerra, C.; Gunnlaugsson, H.P.; Martín-Luengo, A.T.; Schaaf, P.; Bonanni, A.; Masenda, H.; et al. Anisotropy of the Electric Field Gradient in Two-Dimensional α-MoO_3 Investigated by ^{57}Mn(^{57}Fe) Emission Mössbauer Spectroscopy. *Crystals* **2022**, *12*, 942. [CrossRef]
18. Gunnlaugsson, H.P. Spreadsheet based analysis of Mössbauer spectra. *Hyperfine Interact.* **2016**, *237*, 79. [CrossRef]
19. Ziegler, J.F. Interactions of Ions with Matter. SRIM-2008 Software Package. Available online: http://www.srim.org (accessed on 26 March 2023).
20. Papaefthymiou, G.C.; Viescas, A.J.; Le Breton, J.-M.; Chiron, H.; Juraszek, J.; Park, T.-J.; Wong, S.S. Magnetic and Mössbauer characterization of the magnetic properties of single-crystalline sub-micron sized $Bi_2Fe_4O_9$ cubes. *Curr. Appl. Phys.* **2015**, *15*, 417–422. [CrossRef]
21. Sobolev, A.V.; Rusakov, V.S.; Gapochka, A.M.; Glazkoa, I.S.; Gubaidulina, T.V.; Matsnev, M.E.; Belik, A.A.; Presniakov, I.A. ^{57}Fe Mössbauer spectroscopy study of cycloidal spin arrangements and magnetic transitions in $BiFe_{1-x}Co_xO_3$. *Phys. Rev. B* **2020**, *101*, 224409-(1)–224409-(13). [CrossRef]
22. Gütlich, P.; Bill, E.; Trautwein, A.X. *Mössbauer Spectroscopy and Transition Metal Chemistry: Fundamentals and Applications*; Springer: Berlin/Heidelberg, Germany, 2011.
23. Kothari, D.; Reddy, V.R.; Gupta, A.; Phase, D.M.; Lakshmi, N.; Deshpande, S.K.; Awasti, A.M. Study of the effect of Mn doping on the $BiFeO_3$ system. *J. Phys. Condens. Matter* **2007**, *19*, 136202-(1)–136202-(8). [CrossRef]
24. El-Desoky, M.; Ayoua, M.; Mostafa, M.; Ahmed, M. Multiferroic properties of nanostructured barium doped bismuth ferrite. *J. Magn. Magn. Mater.* **2016**, *404*, 68–73. [CrossRef]
25. Das, R.; Mandal, K. Magnetic, ferroelectric and magnetoelectric properties of Ba-doped $BiFeO_3$. *J. Magn. Magn. Mater.* **2012**, *324*, 1913–1918. [CrossRef]
26. Kumar, A.; Denev, S.; Zeches, R.J.; Vlahos, E.; Podraza, N.J.; Melville, A.; Schlom, D.G.; Ramesh, R.; Gopalan, V. Probing mixed tetragonal/rhombohedral-like monoclinic phases in strained bismuth ferrite films by optical second harmonic generation. *Appl. Phys. Lett.* **2010**, *97*, 112903. [CrossRef]
27. Mehedi, H.; Hakim, M.A.; Basith, M.A.; Hossain, M.S.; Ahmmad, B.; Zubair, M.A.; Hussain, A.; Islam, M.F. Size dependent magnetic and electrical properties of Ba-doped nanocrystalline $BiFeO_3$. *AIP Adv.* **2016**, *6*, 035314.
28. Li, M.; Ning, M.; Ma, Y.; Wu, Q.; Ong, C.K. Room temperature ferroelectric, ferromagnetic and magnetoelectric properties of Ba-doped $BiFeO_3$ thin films. *J. Phys. D* **2007**, *40*, 1603–1607. [CrossRef]
29. Godara, S.; Kumar, B. Effect of Ba–Nb co-doping on the structural, dielectric, magnetic and ferroelectric properties of $BiFeO_3$ nanoparticles. *Ceram. Int.* **2015**, *44*, 6912–6919. [CrossRef]
30. Cheng, G.F.; Huang, Y.H.; Ge, J.J.; Lv, B.; Wu, X.S. Effects of local structural distortion on magnetization in $BiFeO_3$ with Pr, Ba co-doping. *J. Appl. Phys.* **2012**, *111*, 07C707. [CrossRef]
31. Jayakumar, O.D.; Achary, S.N.; Girija, K.G.; Tyagi, A.K.; Sudakar, C.; Lawes, G.; Naik, R.; Nisar, J.; Peng, X.; Ahuja, R. Theoretical and experimental evidence of enhanced ferromagnetism in Ba and Mn cosubstituted $BiFeO_3$. *Appl. Phys. Lett.* **2010**, *96*, 032903. [CrossRef]
32. Si, Y.H.; Xia, Y.; Shang, S.K.; Xiong, X.B.; Zeng, X.R.; Zhou, J.; Li, Y.Y. Enhanced Visible Light Driven Photocatalytic Behavior of $BiFeO_3$/Reduced Graphene Oxide Composites. *Nanomaterials* **2018**, *8*, 526. [CrossRef]

33. Quan, Z.C.; Hu, H.; Xu, S.; Liu, W.; Fang, G.J.; Li, M.Y.; Zhao, X.Z. Surface chemical bonding states and ferroelectricity of Ce-doped $BiFeO_3$ thin films prepared by sol–gel process. *J. Sol-Gel Sci. Technol.* **2008**, *48*, 261–266. [CrossRef]
34. Li, Z.J.; Hou, Z.L.; Song, W.L.; Liu, X.D.; Cao, W.Q.; Shao, X.H.; Cao, M.S. Unusual continuous dual absorption peaks in Ca-doped $BiFeO_3$ nanostructures for broadened microwave absorption. *Nanoscale* **2016**, *8*, 10415–10424. [CrossRef] [PubMed]
35. Yiyi, Z.; Chuye, Q.; Yuhui, M.; Qi, W.; Weiwei, M.; Xingfu, W.; Jian, Z.; Yonggang, M.; Jianping, Y.; Xingao, L.; et al. Effect of Eu, Mn co-doping on structural, optical and magnetic properties of $BiFeO_3$ nanoparticles. *Mater. Sci. Semicond. Process.* **2017**, *57*, 178–184.
36. Dutta, D.P.; Jayakumar, O.D.; Tyagi, A.K.; Girija, K.G.; Pillai, C.G.S.; Sharma, G. Effect of doping on the morphology and multiferroic properties of $BiFeO_3$ nanorods. *Nanoscale* **2010**, *2*, 1149–1154. [CrossRef] [PubMed]
37. Burns, S.R.; Paull, O.; Jurasek, J.; Nagarajan, V.; Sando, D. The Experimentalist's Guide to the Cycloid, or Noncollinear Antiferromagnetism in Epitaxial $BiFeO_3$. *Adv. Mater.* **2020**, *32*, 2003711. [CrossRef] [PubMed]
38. Kim, C.S.; Min, B.K.; An, S.Y.; Uhm, Y.R. Mössbauer studies of $Y_3Fe_{4.75}Al_{0.25}O_{12}$. *J. Magn. Magn. Mater.* **2002**, *239*, 54–56. [CrossRef]
39. Kim, C.S.; Min, B.K.; Kim, S.J.; Yoon, S.R.; Uhm, Y.R. Crystallographic and magnetic properties of $Y_3Fe_{5-x}Al_xO_{12}$. *J. Magn. Magn. Mater.* **2003**, *254–255*, 553–555. [CrossRef]
40. Catalan, G.; Sardar, K.; Church, N.S.; Scott, J.F.; Harrison, J.; Redfern, S.A. Effect of chemical substitution on the Néel temperature of multiferroic $Bi_{1-x}Ca_xFeO_3$. *Phys. Rev. B* **2009**, *79*, 212415. [CrossRef]
41. Suresh, P.; Srinath, S. Effect of La substitution on structure and magnetic properties of sol-gel prepared $BiFeO_3$. *J. Appl. Phys.* **2013**, *113*, 17D920. [CrossRef]

Disclaimer/Publisher's Note: The statements, opinions and data contained in all publications are solely those of the individual author(s) and contributor(s) and not of MDPI and/or the editor(s). MDPI and/or the editor(s) disclaim responsibility for any injury to people or property resulting from any ideas, methods, instructions or products referred to in the content.